# BLOCKER-BASED SCATTER CORRECTION FOR CONE-BEAM COMPUTED TOMOGRAPHY

by

CONG ZHAO

Presented to the Faculty of the Graduate School of
The University of Texas at Arlington in Partial Fulfillment
of the Requirements
for the Degree of

MASTER OF SCIENCE IN PHYSICS

THE UNIVERSITY OF TEXAS AT ARLINGTON

May 2015

Acknowledgements

I would like to express my very great appreciation to Dr. Jin for his valuable and constructive suggestions during the planning and development of this research work. I would also like to thank my thesis committees, Dr. Wang and Dr. Chen. I am grateful for their incisive comments and feedback that enriched this thesis.

I have been extremely fortunate to collaborate with many prominent researchers: Luo Ouyang, Dr. Wang. Without their continued efforts and support, I would have not been able to bring my work to a successful completion.

April 17, 2015

Abstract

BLOCKER-BASED SCATTER CORRECTION FOR

CONE-BEAM COMPUTED

TOMOGRAPHY

Cong Zhao, Master

The University of Texas at Arlington, 2015

Supervising Professor: Mingwu Jin

Cone-beam computed tomography (CBCT) imaging is widely used in radiation therapy for treatment planning and image-guided therapy. More x-ray scatter signals are detected by the two-dimensional detector arrays in CBCT than by the one-dimensional detector arrays in fan-beam CT (FBCT). Therefore, scatter contamination significantly degrades the image quality in CBCT and must be corrected for satisfying image quality.

Among numerous scatter correction (SC) methods of cone-beam computed tomography (CBCT), the use of lead-strip blockers is low-cost and easy to implement and holds potential to significantly lower patient radiation dose. In such a method, the signal in the blocked regions is assumed to be the scatter signal and can be used to estimate the scatter signal in the unblocked region. However, this assumption is often violated because of the penumbra effect and detector response effect. In this study, we first investigated a moving-blocker based method to simultaneously estimate the scatter signal and reconstruct the complete volume within the field of view (FOV) from a single CBCT scan. Then we proposed to use deconvolution algorithms to improve scatter estimation of the moving-blocker method. A slanted edge method was used to estimate the point spread function (PSF) of the flat panel detector. The parametric PSF was used

in simulation studies to deconvolve the blurred projection image to remove the finite x-ray source and the detector response effect and to get cleaner scatter signal in the blocked regions.

Our results showed that with laborious parameter tuning, the scatter-induced shading artifacts are substantially reduced in CBCT, and the CT number errors in the selected regions of interest are greatly reduced using the moving-blocker method. The detector response function can be reliably measured and calculated using the slanted edge method. The deconvolved projection image shows better quality, more accurate intensity profiles, and much reduced overall root mean square errors compared to the blurred image in the simulation study. Our experiment results further demonstrate that Wiener and Richardson-Lucy deconvolution methods can significantly improve the scatter estimation compared to the direct inverse filtering method.

Finally, The PSF derived from the slanted edge experiment does not take the penumbra effect into account, and the air-scan data from the CBCT projection images of moving blockers fail to derive a reliable PSF. An experiment to determine the combined penumbra and detector response effect and the ultimate effectiveness of deconvolution methods on scatter correction of CBCT reconstruction will be investigated in future work.

Table of Contents

List of Illustrations

List of Tables

# Chapter 1

## Introduction

CBCT technology has been a very important modality in the field of medical imaging over the last few years. CBCT provides additional information that traditional x-rays will not provide. These kinds of information are helpful in radiotherapy treatment processes. CBCT has many advantages compared to FBCT: (1) The 3D image can provide more accurate information especially the location of certain tissues (2) radiation exposure to the patient is up 10 times less (3) much bigger field of view and much faster scan time (4) smaller size and low device price. However, the scatter contamination in CBCT decreases the reconstruction image quality by introducing artifacts and causing errors for CT numbers. The scatter signal has a 2D distribution and only a small portion can be received by FBCT because of the use of 1D detector arrays. In contrast, CBCT receives most of the scatter signal because of the use of 2D detector arrays.

Scatter contamination is one of the major sources of degradation of CBCT images. It degrades image quality by decreasing the contrast, introducing shading artifacts and causing inaccuracies in the reconstructed CT number. The degraded image makes it difficult to delineate the low-contrast soft tissues, and inaccurate CT number makes the dose calculation of adaptive therapy inaccurate [1,2,3]. Therefore, scatter correction is very important in CBCT imaging.

There are many methods that have been investigated to correct scatter contamination in CBCT, including suppression of scatter signal during the acquisition of projection data using anti-scatter grids and increasing the air gap[4,5-10], and correction of scatter signal in projections using computational methods or special scanning protocols [11-26]. The low frequency distribution feature of the scatter signal[27 28]

makes it possible to use blockers to estimate the scatter. Among scatter correction (SC) techniques, blocker-based methods derive the scatter signal from the blocked regions within the projection data [20-26] and do not suffer the computational intense of Monte Carlo simulation [11-14] or the inability of analytical methods for complex or heterogeneous structures [15-19]. However, the static blocker-based methods have some limitations, such as the requirement of additional measurements for each projection view [20,25], the reduced imaging volume corresponding to the blocked region [21,26], or the inaccuracy caused by the interpolation of primary signal in the blocked regions [24,29]. The recent development by keeping the blocker moving during gantry rotation [30,31] overcomes these limitations and is able to simultaneously estimate the scatter signal and reconstruct the entire volume within the field of view (FOV) from a single CBCT scan. Compared to the primary modulation method [22,32,33], not only the lead strip blockers are low-cost and easy to make, but also the radiation dose can be significantly reduced since about half of the incident x-ray intensity is blocked by moving blockers and statistical compressed sensing reconstruction can compensate for sparse view projections and elevated noise due to scatter subtraction.

In this study, we first investigated the moving blocker method [ 30 31]. The detected signal in the blocked regions is assumed to be the scatter signal. The scatter signal in the unblocked regions was obtained by interpolating the detected signal from the blocked regions. Then the primary signal was obtained by subtracting the interpolated scatter signal from the signal in the unblocked regions. To avoid the inaccuracy caused by the interpolation of primary signal, only the primary signal in the unblocked regions was used to reconstruct the 3D image. Some improvements of CBCT reconstruction images have been obtained in our experiment using a simple phantom.

The excellent performance of this moving blocker method is based on the assumption that the signal in the blocked region is purely scatter signals, at least in the central part. However, this assumption is rarely satisfied for narrow lead strips in reality due to the penumbra effect and the detector response effect. These effects make the signal spread from unblocked regions to the blocked regions. Therefore, the signal detected in the unblocked regions needed to be corrected before it was used to do the interpolation. Then we proposed to model the detector response function (DRF) in the blcoked regions and several image deconvolution methods will be developed for recovering the true scatter signal in the blocked regions. We designed a slanted-edge simulation and an slanted-edge experiment to study these effects. This study will provide a theoretically sound and practically viable solution for the problems faced by the current moving blocker methods. By avoiding labrious parameter tuning, the final reconstruction with scatter correction can be more reliable and robust, which is an important component for its application in clinical practice.

# Chapter 2

## Scatter correction using the moving blcoker method

### 2.1 Moving blocker setup

The moving blocker system for CBCT imaging is shown in Fig. 2-1 [30]. To simplify the process in this study, the blocker strips were shifted manually among 6 positions. The blcoker system consists of equally spaced lead strips aligned along the *v*-direction of the detector. A beam attenuation blocker is inserted between the x-ray source and the phantom, and it moves back and forth along the *u*-direction of the detector as the gantry rotates around the *z*-axis. The signal measured in the blocked regions is assumed to be the scatter signal only, and the signal measured in the unblocked regions is the sum of the scatter signal and the primary signal. The scatter signal in the unblocked regions can be estimated from the blocked regions by using the cubic-spline interpolation. To avoid the penumbra effects of the strips, the region (about 10 pixels wide) adjacent to the edges of the strip are excluded from the scatter estimation in the experimental study. The primary signal is obtained by subtracting the interpolated scatter signal from the signal measured in the unblocked regions. A constrained-optimization-based (CO-TV) algorithm is developed to reconstruct the entire volume within the FOV from the unblocked projection data.

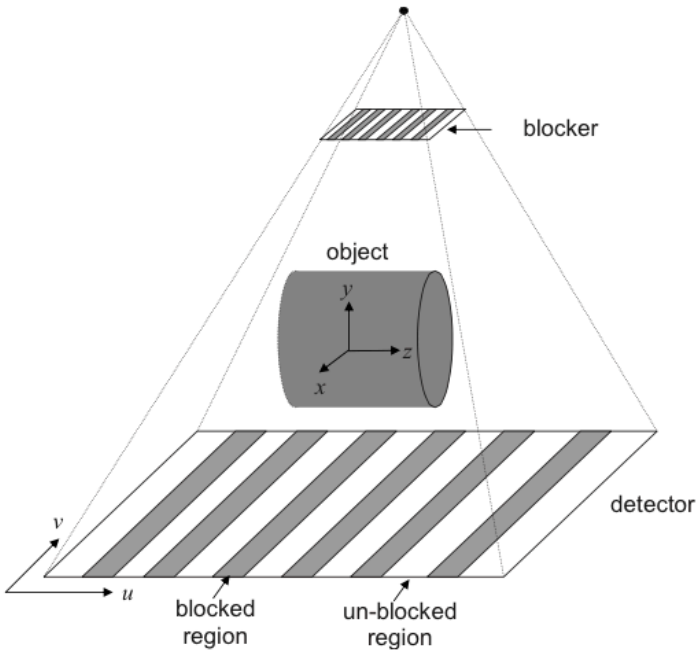


Figure 2-1 moving blocker system

2.2 Data acquisition

The blocker consists of 8 lead strips and the width of each lead strip is 3.2 mm. The lead strips are placed with a 3.2 mm pitch. The blocker is mounted on the F0 bow-tie filter of a CBCT machine. The lead strips of the blocker are aligned perpendicular to the rotation axis and cover the entire FOV all the time at a source-to-blocker distance of 310 mm. The source-to-axis distance is 1000 mm and the source-to-detector distance is 1500 mm. The number of projections for a full 360° rotation is approximately 678 and the total time for acquisition of one full circle of projection data is approximately 2 min. Each projection data contains 1024×768 pixels with a size of 0.388×0.388 $mm^2$. To save computation time during iterative reconstruction, projections were downsampled by a

factor of 2 to yield a size 512×384 with pixel size 0.776 ×0.776 $mm^2$. The tube voltage was 100 kVp and the tube current-time was 0.5 mA s per projection.

A commercial calibration phantom CatPhan® 600 (The Phantom Laboratory, Inc., Salem, NY) was used to evaluate the performance of the proposed method. Six CBCT scans were performed while the phantom was kept stationary. During each scan, the blocker was shifted 1 mm along the *u*-direction. To simulate continuous motion of the blocker during gantry rotation, the projection data of a single CBCT scan were selected from one of the six scans according to the following rule. For the *n*th projection data, let *a* denote the remainder after *n* is divided by 12. If *a* is smaller than 6, the *n*th projection data are chosen from *a*th of those six data sets; if *a* is larger than or equal to 6, the *n*th projection data are chosen from (12−*a*)th of those six data sets. By such a choice, the complete projection data set corresponds to a blocker moving at 1 cm/s.

### 2.3 Constraint optimization reconstruction algorithm

When the blocker strips are used in projection data acquisition, the projection data are partially blocked at every projection and the total amount of projection data is smaller than in a normal CBCT scan. Iterative image reconstruction algorithms have the potential to substantially improve CBCT image quality from limited projection data. [34–36] Recent development of the compressed sensing theorem[37] has demonstrated that a signal can be exactly reconstructed from highly undersampled measurements. Several algorithms based[34–36] on the compressed sensing theorem have been proposed for CT image reconstruction from undersampled projections. In this work, image reconstruction from partially blocked projection data is formulated as a constraint optimization (CO) model under the framework of compressed sensing. Constraint optimization

incorporates data fidelity and image constraints such as positivity, extreme values, and regularity measure. The constraint optimization generates a discrete image $\mu$ by minimizing certain functions of the image

$$\mu^* = arg\ min(f(\mu)) \quad (2.1)$$

subject to the inequality constraints data fidelity and positivity:

$$|A\mu - p| \leq \varepsilon \quad (2.2)$$

$$\mu \geq 0 \quad (2.3)$$

where $p$ is the vector of log-transformed projection measurements after scatter correction and $\mu$ is the vector of attenuation coefficients to be reconstructed. $\varepsilon$ is the tolerance to enforce the data fidelity constraint which accounts for the inconsistency of the measured data such as noise and geometric deviation of the system matrix $A$. The element $a_{ij}$ of the matrix $A$ is the length of the intersection of projection ray $j$ with pixel $i$ and $a_{ij}$is calculated by Siddon's ray-tracing technique[38]. $f(\mu)$ is the prior knowledge imposed on the image and usually measures certain properties of the $\mu$ to be reconstructed. In this work, the total variation (TV) of the image is chosen as the regularity measure of $\mu$

$$f(\mu) = \sum_{x,y,z} \sqrt{(\mu_{x,y,z} - \mu_{x-1,y,z})^2 + (\mu_{x,y,z} - \mu_{x,y-1,z})^2 + (\mu_{x,y,z} - \mu_{x,y,z-1})^2} \quad (2.4)$$

In the following, we refer to the method described above as CO-TV. The constraint in Eq. (2.2) is enforced by the standard algebraic reconstruction technique (ART)

$$\mu_i^{(k+1)} = \mu_i^{(k)} + \lambda a_{ij}\left[\frac{p_j - \sum_i a_{ij}\mu_i^{(k)}}{\sum_i a_{ij}^2}\right] \qquad (2.5)$$

where $k$ is the iterative step and $\lambda$ is the relaxation factor which was chosen as 0.1 in this study. The objective function of Eq. (2.1) is minimized by the standard steepest gradient descent method

$$\mu^{(k'+1)} = \mu^{(k')} - \gamma \nabla f(\mu) \qquad (2.6)$$

where $\nabla f(\mu)$ is the gradient of function $f(\mu)$ and $k'$ is the iteration step. $\gamma$ is the step size and it is updated by steepest decent direction (line 15–19 in the pseudocode of [36]). To avoid a singularity in calculating $\nabla f(\mu)$, a small constant was added to the term inside the square root in Eq.(2.4). After each ART operation of Eq. (2.5), the resulting image is updated according to Eq. (2.6). The number of iterations for the steepest gradient descent step is set to 10 and the number of iterations for the ART step is set to 20 in this study [34,36,39].

## 2.4 Scatter correction scheme

This section shows some pre-processing steps and how the scatter correction method works. During the moving blocker CBCT acquisition, detected signal in the blocked regions is assumed to be attributed to scatter photons only, while the measured signal in the unblocked regions is contributed by both primary and scattered photons. Previous studies [27,28] have showed that the scatter signal of CBCT projection is smooth and low-frequency signal. Here, the scatter signal detected in the blocked region was used to estimate the scatter fluence of the unblocked region using cubic-spline interpolation. To avoid the penumbra effect of the strips, data from regions adjacent to the edges of the strips were excluded, and only the central one-third of each blocked region was used in the scatter estimation in the experimental study. Before interpolation, a 3 × 3 median filter was applied to exclude extremity values of the measured scatters. A 1D 9-pixel moving average filter perpendicular to the lead strips was also used to further smooth the interpolated scatter maps [25,52]. Primary signal in unblocked region was obtained by subtracting the estimated scatter signal. A line integral of each ray in unblocked region was then calculated by the logarithmic transform. To obtain accurate line integrals, a normalization scan (air scan) was acquired without the blcoker. Image reconstruction was then performed on the corrected unblocked partial projection data.

Fig. 2-2 and Fig. 2-3 show an example projection image of air scan and Catphan scan respectively. The intensity of the projection image with blocker is decreased compared to the projection image without blocker, which can reduce the dose of radiation.

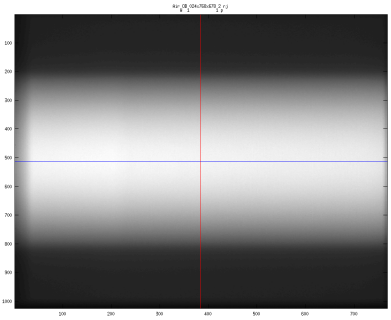

(a) air scan without blcoker

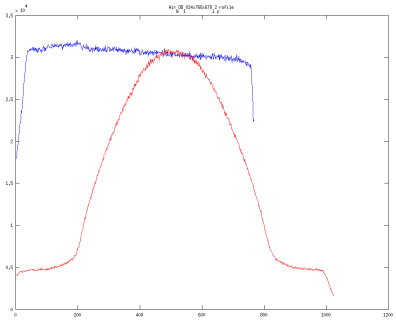

(b) selected profile

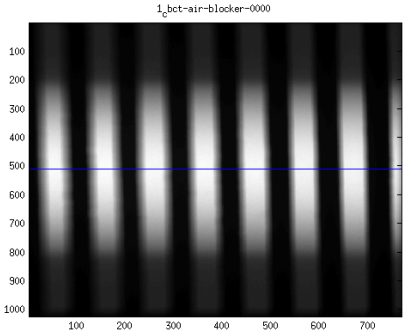


(c) air scan with blocker

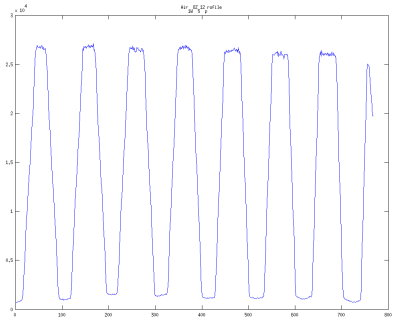

(d) selected profile

Figure 2-2 air scan

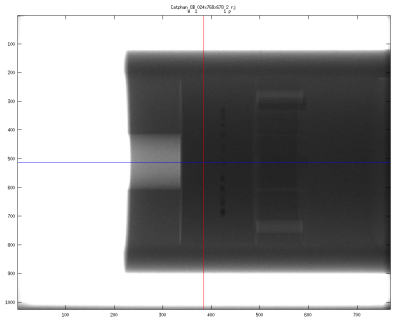

(a) Catphan without blocker

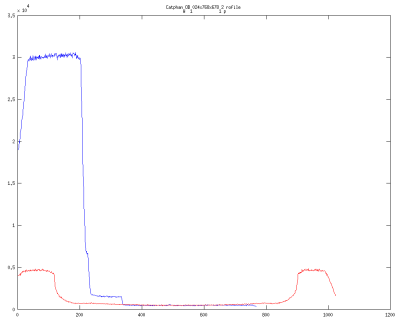

(b) corresponding profile

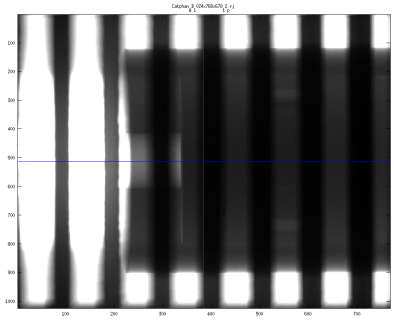

(c) Catphan with blocker

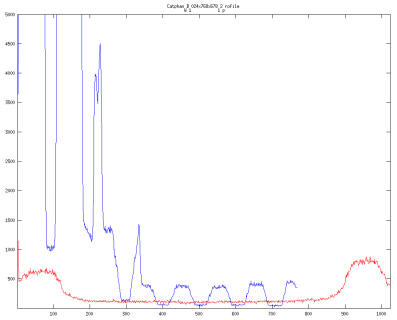

(d) corresponding profile

Figure 2-3 Catphan scan

Fig. 2-4 shows how to estimate scatter signal from blocked regions. The blue line in (a) is the interest of region of measured signal, which is the sum of primary and scatter signal. The red line in (b) is the scatter signal we estimated in the blocked regions, and the estimated scatter signal in unblocked regions is interpolated in (c). Then the black line in (d) is the scatter corrected signal, which obtained by subtracting the red line from the blue line.

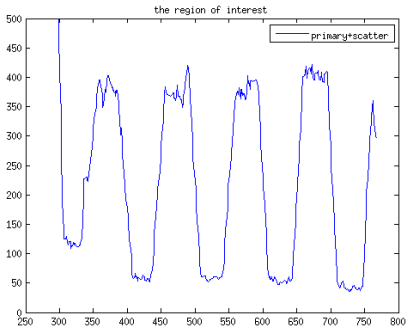


(a) profile of measured signal

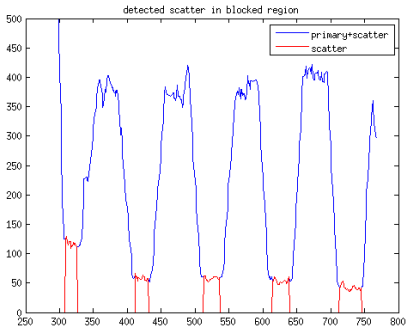


(b) estimated scatter signal

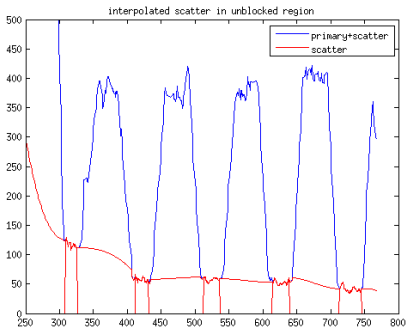


(c) interpolated scatter signal

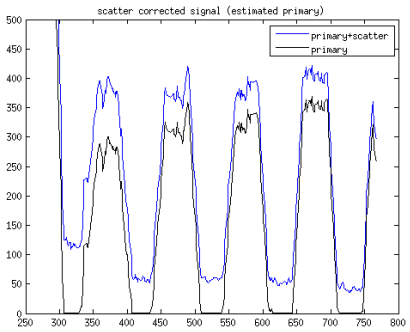


(d) scatter corrected signal

Figure 2-4 scatter correction

2.5 Reconstruction results

This section provides reconstruction results that illustrate the performance of the moving blocker method for scatter correction. We compare the axial images of the sensitometry module of moving blocker method to three competing methods in Figure 2-4. To evaluate the accuracy of the reconstructed CT number in the CBCT images, we calculated the mean CT number of seven ROIs within the sensitometry module. We also acquired fan-beam multidetector CT (MDCT) images of the CatPhan® 600 phantom using a GE Discovery CT scanner (GE Medical Systems, Milwaukee, WI). The CT numbers from MDCT were used as the standard for comparison. The inaccuracy of CT number in CBCT was quantified by the root mean square error (RMSE) in the selected seven ROIs

$$RMSE = \sqrt{\sum_{k=1}^{7}(CT_{cone}^{k} - CT_{fan}^{k})^2} \quad (2.7)$$

where $CT_{cone}^{k}$ and $CT_{fan}^{k}$ denote the mean CT number of the *k*th ROI for CBCT and fan-beam CT, respectively. Table 2-1 lists the CT numbers of different ROIs in Fig. 2-5. The CT numbers of different ROIs for eleven successive slices are shown in Fig. 2-6 to Fig. 2-12. Table 2-2 lists the RMSE of CT numbers of different ROIs for seven successive slices. The RMSE of the CT number in the CBCT images without scatter correction is 130. Using the proposed scatter correction strategy, the RMSE of the CT number is reduced to around 20 in all of the images reconstructed by different methods.

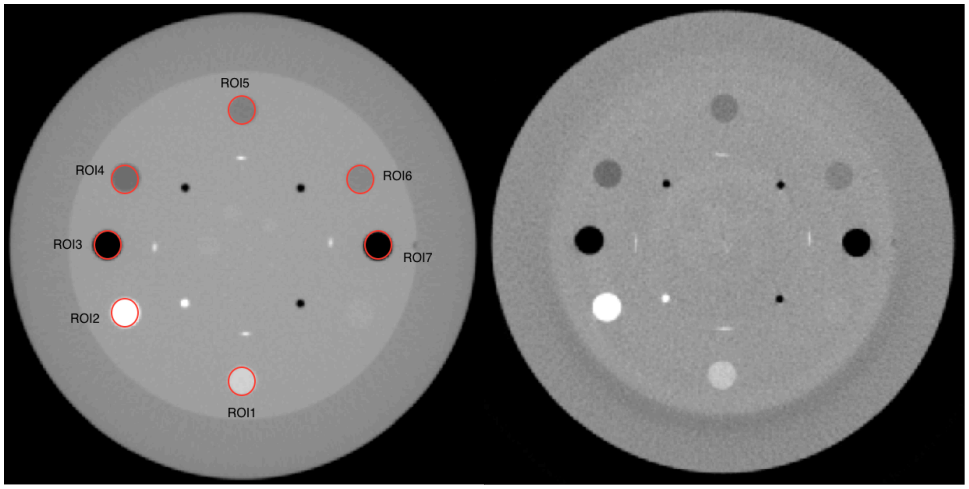


(a) MDCT (b) CBCT

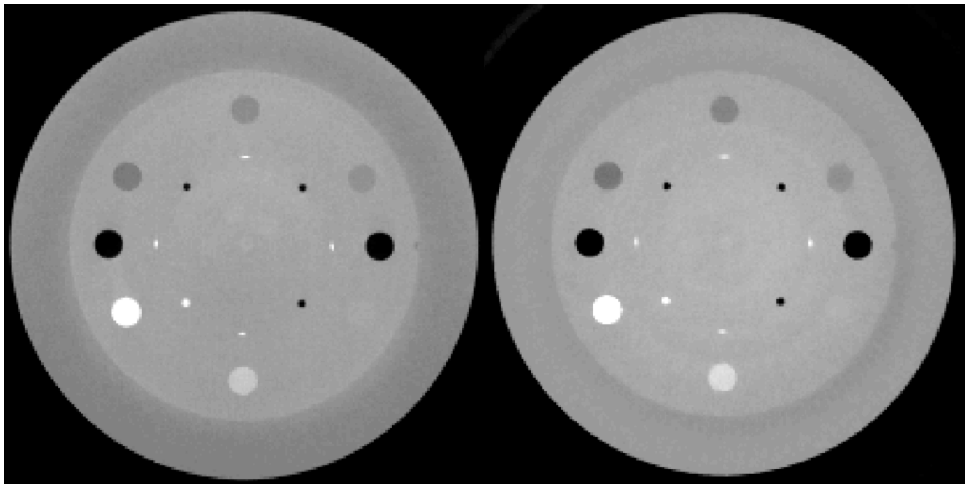

(c) No scatter correction (d) Scatter correction

Figure 2-5 One axial slice of the Catphan 600 phantom sensitometry module

The selected slice image shown above: (a) benchmark fan-beam MDCT image; (b) reconstruction imge from CBCT machine; (c) CO-TV from unblocked projection data; and (d)CO-TV from partially blocked projection data. ROIs labeled in (a) were used for evaluating CT number accuracy. Display widow [−800, 600] HU.

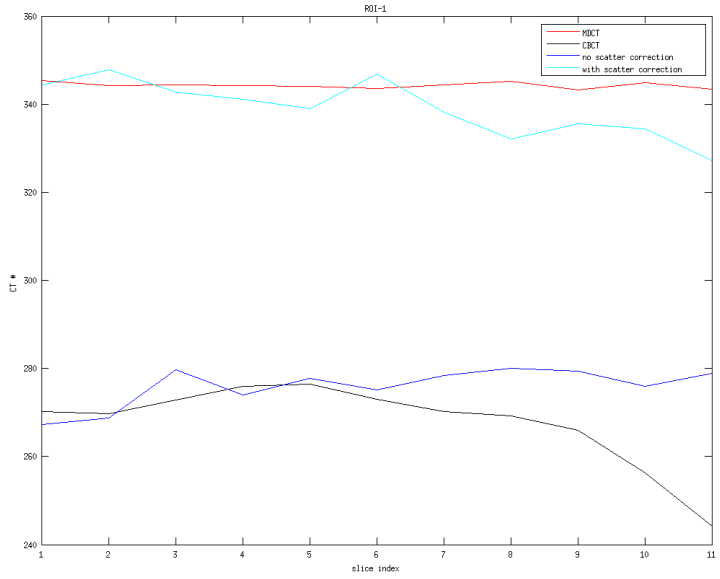


Figure 2-6 CT numbers of ROI-1

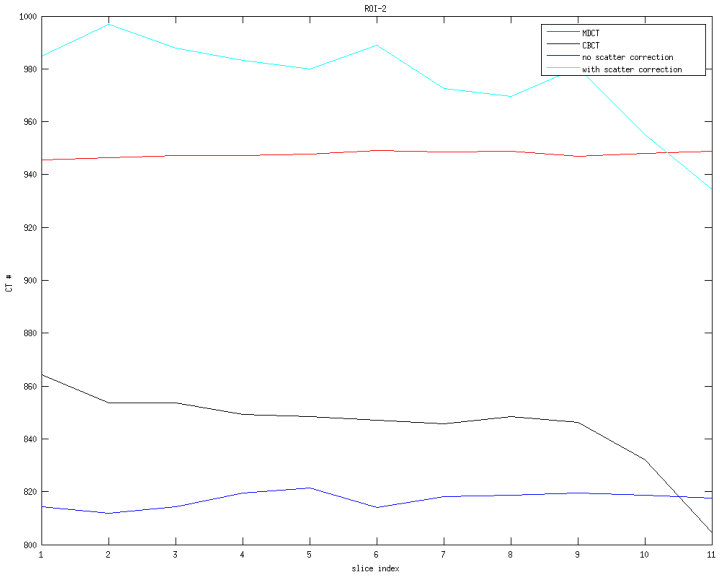


Figure 2-7 CT numbers of ROI-2

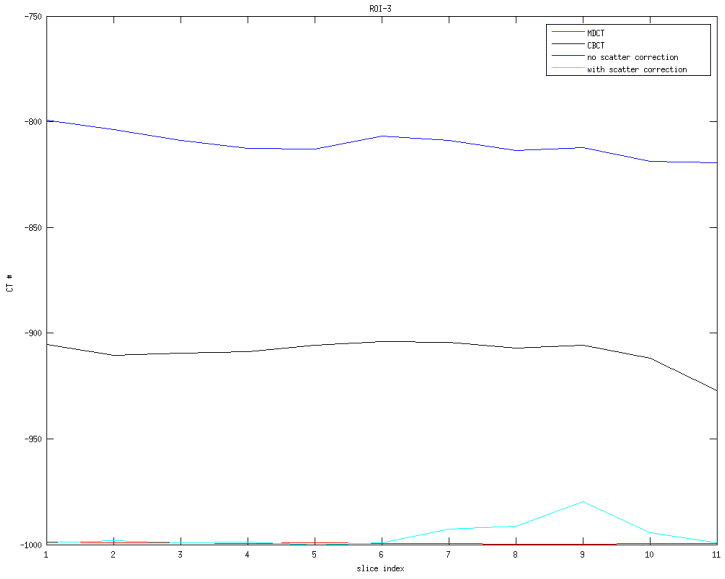


Figure 2-8 CT numbers of ROI-3

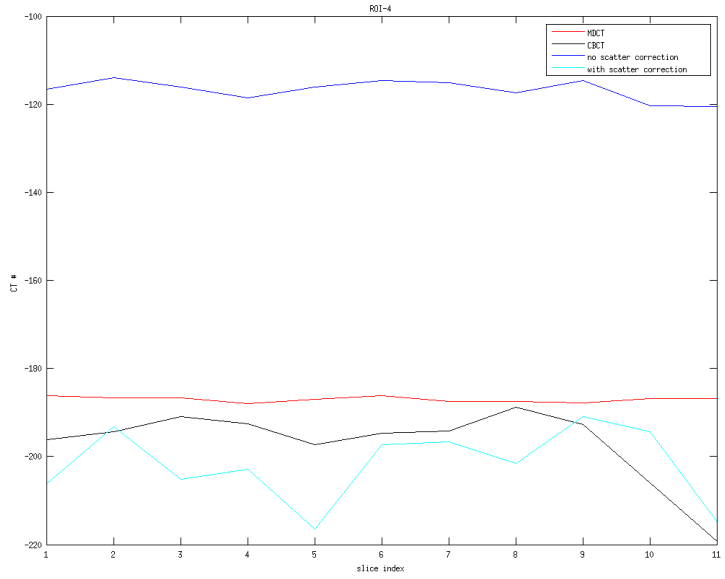


Figure 2-9 CT numbers of ROI-4

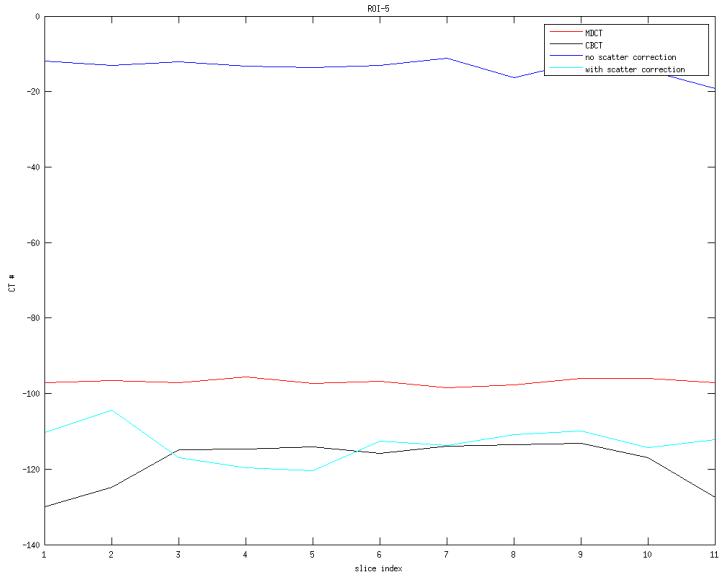


Figure 2-10 CT numbers of ROI-5

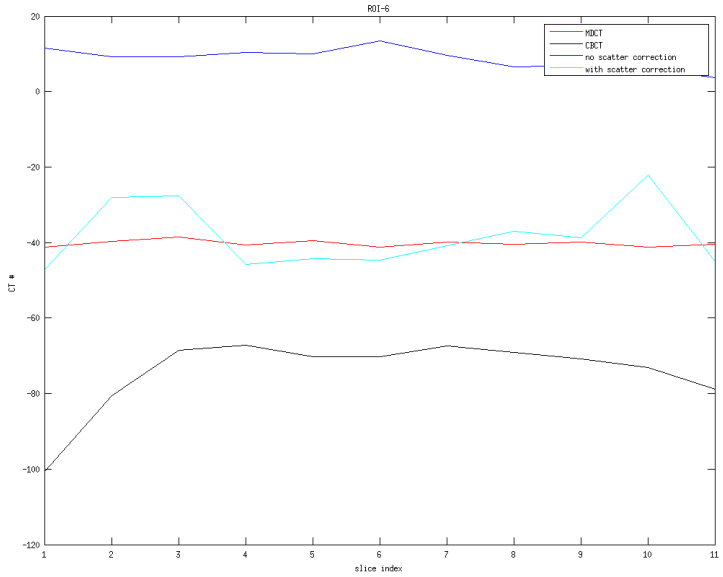


Figure 2-11 CT numbers of ROI-6

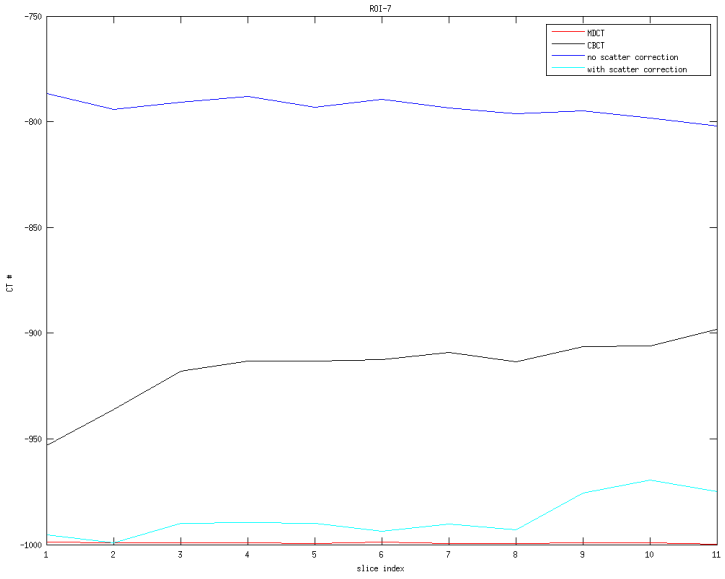


Figure 2-12 CT numbers of ROI-7

Table 2-1 Comparison of the CT number of seven ROIs of the Catphan 600

| | ROI-1 | ROI-2 | ROI-3 | ROI-4 | ROI-5 | ROI-6 | ROI-7 | RMSE |
|---|---|---|---|---|---|---|---|---|
| MDCT | 344 | 948 | -999 | -187 | -97 | -39 | -999 | |
| CBCT | 273 | 847 | -904 | -195 | -116 | -70 | -913 | 70 |
| No SC | 270 | 820 | -800 | -124 | -15 | 10 | -780 | 130 |
| SC | 332 | 970 | -991 | -202 | -111 | -37 | -993 | 20 |

Table 2-2 RMSE of CT numbers of different ROIs for seven successive slices

| Slice number | 1 | 2 | 3 | 4 | 5 | 6 | 7 |
|---|---|---|---|---|---|---|---|
| CBCT | 63 | 63 | 65 | 66 | 67 | 68 | 69 |
| No SC | 132 | 130 | 128 | 128 | 126 | 130 | 128 |
| SC | 17 | 20 | 19 | 17 | 19 | 16 | 12 |

## 2.6 Conclusion

The results of RMSE show that the moving blocker scatter correction method is effective. However, the scatter signal in this experiment had to be carefully extracted by avoiding the edge pixels and a scaling was needed most time to compensate the spread of signal from unblocked regions for a good scatter correction performance. Therefore, we proposed a slanted-edge method to avoid these drawbacks in next chapter.

# Chapter 3

## A simulation study

This chapter shows a simulation study of several deconvolution methods for deblurring image.

### 3.1 Blocker-based scatter correction for CBCT and mathematical models

The fundamental assumption in blocker-based scatter estimation lies on:

$$S^{ideal}(u,v)\begin{cases} S_{p(u,v)} + S_{s(u,v)}, & (u,v) \in blocked\ region \\ S_{s(u,v)}, & (u,v) \in unblocked\ region \end{cases} \tag{3.1}$$

where $S^{ideal}(u,v)$ is the "ideally" measured signal, $S_{p(u,v)}$ is the primary signal and $S_{s(u,v)}$ is the scatter signal. Since in the blocked regions the signal is deemed purely scatter and the scatter is a low-frequency signal at least in longitudinal direction [25], the scatter in blocked region can be estimated through interpolation of signals in blocked region. Then, the primary signal in unblocked region can be recovered by subtracting estimated scatter signal from measured total signal and used for reconstruction. However, the assumption of pure scatter in blocked regions is usually violated in reality. As demonstrated by the air scan of the blocker (without the object in Fig 1) in Fig 2-2, the edges between blocked and unblocked regions do not show a vertically straight transition from high intensity to low intensity. In addition, significantly amount of signal still exists in the blocked region, which should be (close to) zero by the assumption. Therefore, the scatter signal in the previous experiment had to be carefully extracted by avoiding the edge pixels and a scaling was needed most time to compensate the spread of signal from unblocked regions for a good scatter correction performance [30,31].

In this study, we will investigate the sources for the contamination of scatter in blocked regions and propose several methods to extract more faithful scatter signals

without empirical parameter tuning. If we assume an ideal point x-ray source and no detector veiling/scatter glare, the detect signal can be described as

$$S^{ideal}(u,v) = S_{p(u,v)} \sum_{i=1}^{k} \Pi\left(\frac{u-u_i}{w}\right) + S_s(u,v) \qquad (3.2)$$

where the primary signal is $S_{p(u,v)} = I_0 e^{-\int_L \mu(x,y,z)dl}$ with the uniform source intensity $I_0$ and the ray path *L* from the source to the point *(u,v)* on the detector, $S_{S(u,v)}$ is the object scatter signal that can be modeled as a convolution of incident fluence and the scatter kernel [17]. $\Pi(\bullet)$is the standard rectangular function (1 inside the window and 0 outside) and $\sum_{i=1}^{k} \Pi\left(\frac{u-u_i}{w}\right)$ represents the ideal projection image of *K* blockers (with the center $\mu_1$and the width *w*) on the detector. Note that blocked regions are outside the rectangular windows. This equation is equivalent to Eq. (3.1).

However, the real measured signal does not exactly follow Eq. (3.2) as can be seen in Fig. 2-1. At least two major blurring factors have to be taken into account: 1) the response function of the flat panel detector (FPD); and 2) the penumbra effect due to the finite x-ray source distribution. (Note that the diffraction effects can be neglected because the x-ray wavelengths are very small ($\sim 10^{-11}$ m) and the width of the blocker is several millimeters. Thus, under the usual CBCT imaging setup, Fresnel number is much greater than one, which does not satisfy the condition to generate a bright spot behind the blocker.) Therefore, if assuming linear shift invariant (LSI) for both effects, the measured data can be expressed as:

$$S_{(u,v)} = S^{ideal}(u,v) \otimes PEF(u,v) + n(u,v) \qquad (3.3)$$

$$= S_p(u,v) \sum_{i=1}^{k} \Pi\left\{\frac{u-u_i}{w}\right\} \otimes DRF(u,v) \otimes PEF(u,v) + n(u,v)$$

where ⊗ denotes convolution, DRF(u,v) is the point spread function of the FPD, PEF(u,v) models the blurring due to the penumbra effect, $S_S^*(u,v)$ is the object scatter signal in Eq. (3.2) convolved by DRF(u,v) and PEF(u,v), and $n(u,v)$ is the detector electronic noise. It is straightforward to see that the signal reaching the FPD will be blurred by DRF. The blurring effect from PEF comes from the source distribution that can be modeled as convolution of an ideal point source (see Eq. (3.6)). Comparing Eq. (3.3) with Eq. (3.2), we can see that the primary signal can spread outside the rectangular windows and cause the contamination of the scatter signal in unblocked regions. Although the blocker width may be increased to mitigate this contamination, practically this is not desired because it will compromise the primary signal coverage and deteriorate the reconstruction.

The primary goal of this work is to use deconvolution methods to recover the ideal signal $S^{ideal}(u,v)$ in Eq. (3.2) from the measured signal $S_{(u,v)}$ in Eq. (3.3). Consequently, the signal in the blocked regions (i.e. outside the window function) can better represent true scatter (at least in the central part of the region), which will lead to more accurate estimate of the primary signal for reconstruction.

## 3.2 Models of the detector response and the penumbra effect for blocker-based imaging

### 3.2.1 Modeling detector response function (DRF)

An ideal point x-ray beam will generate a spread in the FPD due to the effects of radiation scatter, light diffusion, and charge sharing etc. Since the ideal point beam is hard to achieve, the slanted-edge method [41,42] will be used to estimate the detector response function (DRF), i.e. point spread function [43,44]. A lead sheet with sharp and straight edge will be placed directly on the top of the FPD to avoid off-focal radiation and

environmental scatter. A uniform incident fluence on the measured area will be assured by calibration. The angle of the edge is not parallel to the u or v axis, but slanted slightly (<5°). This allows the gradient of the edge to be measured at various phases relative to the detector element and generates an oversampled edge profile as shown in Fig. 3-1, which will provide extra high frequency response information.

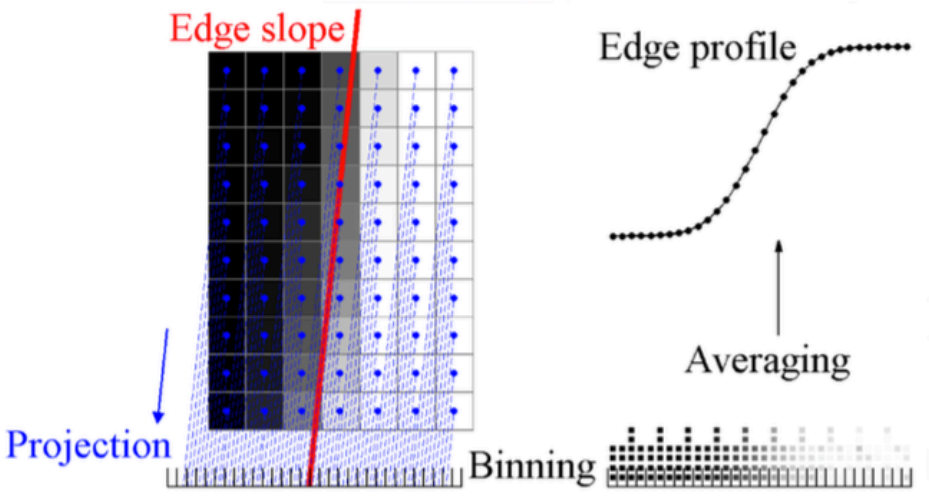


Figure 3-1 Edge response function estimation using the slanted edge method

The empirical line spread function (LSF) can be obtained by taking the derivative of the edge profile. The empirical LSF will be further fitted to the following parametric function:

$$LSF^{fit}(u) = \frac{a_1}{\sqrt{2\pi b_1^2}} e^{-u^2/2b_1^2} + \frac{a_2}{\pi b_2^2}|u|K_1\left(\frac{|u|}{b_2}\right) + \frac{1-a_1-a_2}{\pi b_3}\frac{1}{1+u^2/b_3^2} \qquad (3.4)$$

where $K_1(\bullet)$ is a first-order modified Bessel function. This function is proposed to model the long tail of LSF and the weighted least squares can be used to find the parameters

[43]. The LSF will be measured and calculated at multiple positions on the detector with both u and v directions to make sure that the DRF of FPD is spatial invariant and rotationally symmetric. Given rotational symmetry, the DRF can be expressed as:

$$DRF^{fit}(r) = \frac{a_1}{\sqrt{2\pi b_1^2}} e^{-u^2/2b_1^2} + \frac{a_2}{2\pi b_2^2} e^{-r/b_2} + \frac{1-a_1-a_2}{2\pi b_3} \frac{1}{(1+r^2/b_3^2)^{3/2}} \qquad (3.5)$$

where r is equal to$\sqrt{u^2+v^2}$. In Eq. (3.5), it is tempting to attribute the three terms as modeling the distributions of the incident intensity in the scintillator, the diffusion of scattered optical photons, and the scatter of x-ray photons in the detector panel and housing, respectively [43]. However, we treat them as a general description of a point spread function with variable tail effects, i.e. the short range for the first Gaussian term, the medium range of the exponential term, and the long range of the polynomial (Lorentzian) term.

### 3.2.2 Modeling penumbra effect function (PEF)

The finite size of x-ray focal spot (inside the full width half maximum (FWHM) of the source, <1 mm) and the off-focal-spot radiation (outside the FWHM of the source with non-negligible radiation, ~several mm) produce the penumbra effect of the blockers. This effect results in different $I_0$ values as shown in Fig. 3-2, where the black region on the detector is totally blocked by the blocker (when ignoring the detector response in Chapter 3.1), the green ones are unblocked, so called umbras, and the red ones are partly shun by x-ray, so called penumbras.

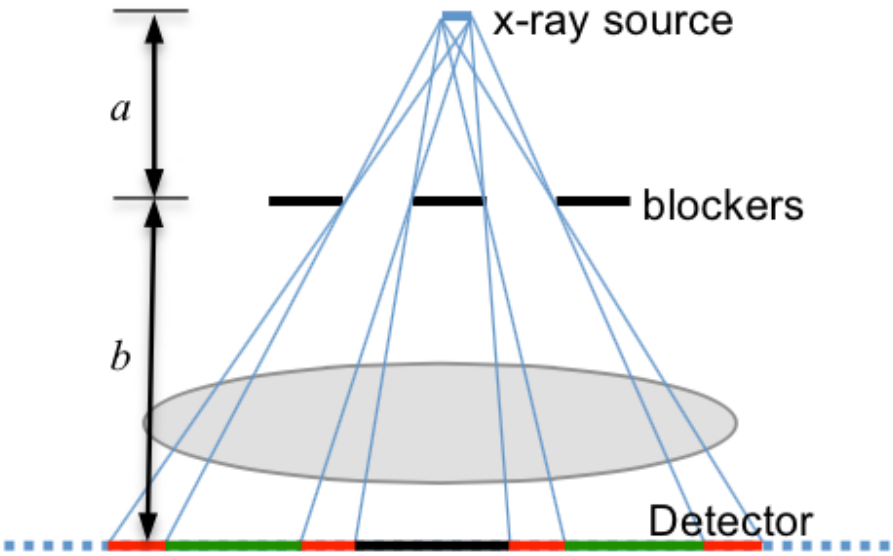


Figure 3-2 Edge response function estimation using the slanted edge method

Given the focal spot length $L_f$ , the source to the blocker distance $a$, and the blocker to the detector distance $b$, the penumbra size can be computed as $L_p = (bL_f)/a$ . If the blockers have the equal width and spacing, denoted as $d$, an ideal point source (i.e. an infinitesimally small source) would result in a uniform alternating pattern of the blocked and unblocked regions on the detector with the equal size of $L_I = d(a+b)/a$ , which is the sum of one black (or green) region and one red region. Given a typical values of $L_f$=0.4 mm, $a$ =300 mm, $b$ = 1200 mm, and $d$ =3 mm [31, 45], $L_p$ is 1.6 mm and $L_I$ is 15 mm. Therefore, the penumbra could take more than 10% of the ideally blocked region even by considering only the finite size of the focal spot. If taking the off-focal-spot radiation into account, which is in the same order of the size of the blocker, the penumbra effect region could be ten-fold greater and spread to the whole blocked region [45]. Following the recent study of penumbra effect of the collimator blades, we can model the actual incident intensity $L_A$ as

$$I_A(u,v) = I_0 \otimes f(u\bullet a/b,\ v\bullet a/b) = I_0 \otimes PEF(u,v) \qquad (3.6)$$

$I_0$ has the uniform value inside the illuminated area and 0 outside, and $f$ is the x-ray source distribution. The penumbra effect function (PEF) is then defined as the source distribution magnified on the detector by a factor of $b/a$. Note that the penumbra effect of the collimator blades is around the borders of FOV and can be ignored compared to that of the blockers in the regions of interest. Although the off-focal-spot radiation is generally small, it significantly contributes to the spread due the convolution on a large off-focal-spot area in Eq. (3.6).

The pinhole method will be used for the measurement of source distribution because it is easy to implement and able to provide 2D distribution [45,46]. Briefly, A standard pinhole assembly is attached to the surface of the field collimator. After calibration, the focal spot, pinhole, and the center of detector are aligned, and a magnified image of the focal spot is projected onto the detector. The background signals measured by blocking the pinhole are subtracted from the pinhole measurement to get the clean distribution of the source on the detector by assuming a negligible DRF influence on PEF. The deconvolution methods described in next section will be used to test the negligible DRF influence hypothesis. If the pinhole method cannot provide satisfying measure of PEF, advanced coded aperture methods can be used [47]. Assuming a rotational symmetry, a similar parametric function Eq. (3.5) can be used to break down PEF into different spread range factors.

## 3.3 Recovery of true scatter in blocked regions

Once we accurately estimate DRF and PEF based on Eq. (3.5), the deconvolution techniques can be used to recover true scatter in blocked regions, i.e. to reverse the effect of DRF and PEF in Eq. (3.3) so that Eq. (3.2) can be satisfied to a maximum extent and the estimation of scatter in unblocked region can follow the routine. In the following context, we denote $F(\bullet)$ as Fourier transform of the function from the spatial domain to the spatial frequency domain, and $F^{-1}(\bullet)$ as inverse Fourier transform. The multiplication, division and comparison involving an array (e.g. $S$, $S^{ideal}$ and their Fourier transform) are element wise, unless otherwise stated.

### 3.3.1 Inverse and Wiener filtering

The most straightforward method is the inverse filtering. In this method, the derived DRF and PEF are transformed into the spatial frequency domain, denoted as $\mathcal{F}$(DRF) and $\mathcal{F}$(PEF), so is the measured signal S, $\mathcal{F}$(S). Then, the recovered signal can be expressed as $\tilde{S}^{ideal} = \mathcal{F}^{-1}(\frac{\mathcal{F}(\mathrm{S})}{\mathcal{F}(\mathrm{DRF})\mathcal{F}(\mathrm{PEF})})$. It is well known that the direct inverse filtering will produce the high frequency ringing artifacts. Since the contamination in the central part of the blocked region can be only introduced by the long tails of DRF and PEF, which can be represented by the last two terms (exponential + Lorentzian) or the last one term (Lorentzian), denoted as $\mathrm{DRF}^{\mathrm{LT}}$ and $\mathrm{PEF}^{\mathrm{LT}}$, the inverse filtering can be achieved by $\tilde{S}^{ideal} = \mathcal{F}^{-1}(\frac{\mathcal{F}(S)}{\mathcal{F}(\mathrm{DRF})\mathcal{F}(\mathrm{PEF})})$ instead. As shown in [43], this process can effectively remove the long tail effect of the detector scatter without introducing new artifacts. We expect the similar performance for the long tail effect of the penumbra.

The electronic noise term n(u,v) in Eq. (3.3) can be modeled as a Gaussian white noise and its power spectral function (PSF) can be estimated from either the flood field or the dark image. The Wiener deconvolution can be expressed as

$$\tilde{S}^{ideal} = \mathcal{F}^{-1}\left(\frac{\mathrm{H}^{*}\bullet PSF(\mathrm{S})}{|H|^{2}\mathrm{PSF(S)}+\mathrm{PSF(n)}}\right) \qquad (3.7)$$

where $H = \mathcal{F}(DRF)\mathcal{F}(PEF)$ or $\mathcal{F}$ (***DRF*** $^{LT}$ ) $\mathcal{F}$ ( ***PEF*** $^{LT}$ ), * denotes the complex conjugate, and PSF(S) and PSF(n) are power spectral functions of the signal S and n, respectively.

3.3.2 Maximum likelihood estimate using the Richardson-Lucy algorithm

From Eq. (3.3), the ideal signal $S^{ideal}$ consists of both the primary and scatter signals, which follow Poisson distribution and is blurred by a known point spread function, *h* = ***DRF*** ⊗ ***ERF*** . The maximum likelihood estimate of $S^{ideal}$ given the measurements S and *h* can be obtained using the iterative Richardson-Lucy algorithm [48,49] as follows

$$S^{ideal(t+1)} = S^{ideal(t)}\left(\frac{S}{S^{ideal(t)}\otimes h}\otimes\hat{h}\right) \qquad (3.8)$$

where S $^{ideal(t)}$ and S $^{ideal(t+1)}$ are estimate of S $^{ideal}$ at t $^{th}$ and (t+1) $^{th}$ iteration, respectively, and $\hat{h} = h(-u,-v)$ . In case of high noise, e.g. the blocked region with low statistical counts, a regularization term, denoted R(S), can be added to the Richardson-Lucy algorithm [50,51]. The iteration can be modified by adding a scaling factor, $(1-\lambda \mathrm{div}(R(S^{ideal(t)})))^{-1}$, to the right side of Eq. (3.8), where div is the divergence of the regularization function R(S). Different regularization functions, such as $L_2$ norm, total variation (TV) norm, and

Huber-norm, will be tested if the regularization is necessary although the use of heuristic parameter is generally avoided.

### 3.4 Model validation and evaluation of scatter recovery methods

To investigate whether deconvolution methods can improve the scatter estimation under different blurring and noise conditions for blocker-based methods for CBCT. An “ideal” projection image with scatter was first simulated for blocker-based CBCT data acquisition by assuming no blurring effect and no noise. The ideal image was then convolved with long-tail PSF with different width to mimic the blurring effect from the finite focal spot and detector response. Different levels of noise were also added. Three deconvolution methods: 1) inverse filtering; 2) Wiener; and 3) Richardson-Lucy, were used to recover the scatter signal in the blocked regions. The root mean square error (RMSE) of estimated scatter serves as a quantitative measure for the performance of different methods under different blurring and noise conditions.

### 3.5 Simulation results

The phantom we simulated is from one of the projection image of CBCT, and six black strips is applied as blocker strips in Figure 3-3 (b). The size of the phantom is 1024*768 with the 0.388 mm pixel size. Then we generated a 2D scatter signal (d), which is generated from a Gaussian function (sigma=600). By adding the scatter signal to the projection image, we obtained the profile with scatter contamination(e).

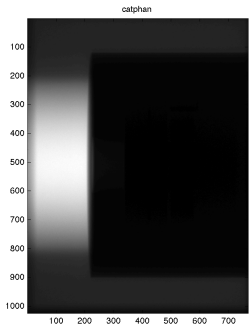


(a) projection image

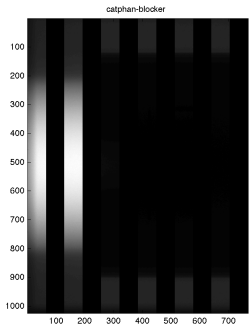


(b) applied blocker

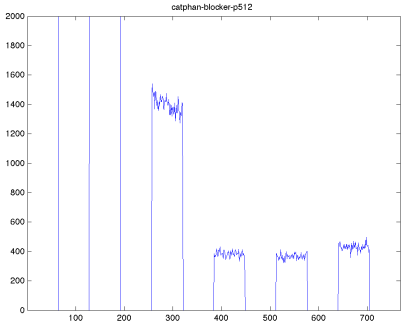


(c) profile without scatter

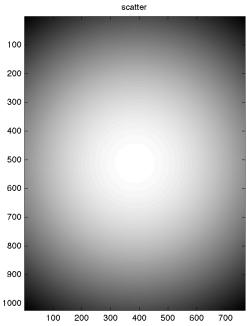


(d) generated scatter signal

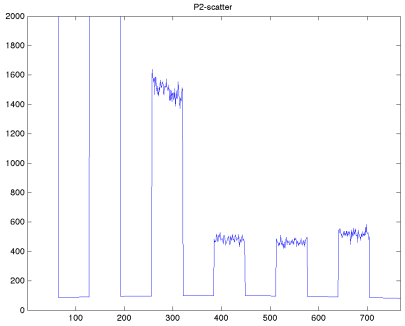


(e) profile with scatter

Figure 3-3 Simulated phantom and scatter signal

There are 5 different width of PSF that are simulated using Eq. (3.5). The size of the PSF is 81*81 pixels (0.388 mm pixel size). We choose the full width tenth maximum (FWTM) as the width of the PSF. The corresponding FWTM is 0.155mm, 6.2 mm, 12.4 mm, 18.6 mm and 24.8 mm respectively and first two of them are shown in Fig. 3-4.

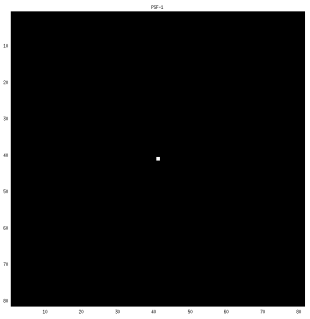

(a) PSF-1

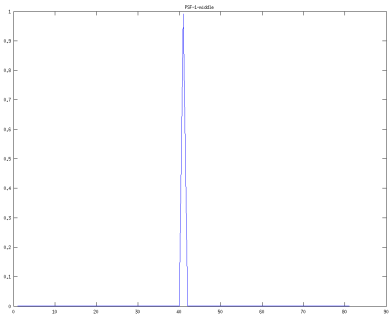

(b) LSF

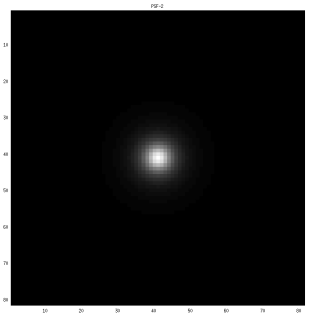

(c) PSF-2

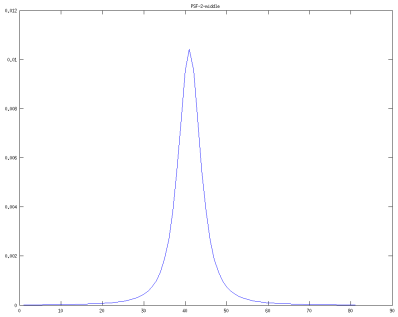

(d) LSF

Figure 3-4 two different PSF and the corresponding LSF

There are five different level of noise are added to the image after they convolved the five PSF. They are defined as signal-to-noise ratio (SNR) at 160dB, 80dB, 40dB, 20dB and 10dB (i.e. 0.0001%, 0.01%, 1%,10% and 20% noise).Two convovled image and selected profile are shown in Fig. 3-5. The sharp edge became smooth because of the blur effect of the convolution.

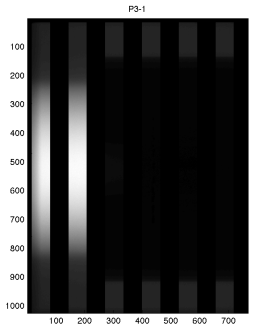


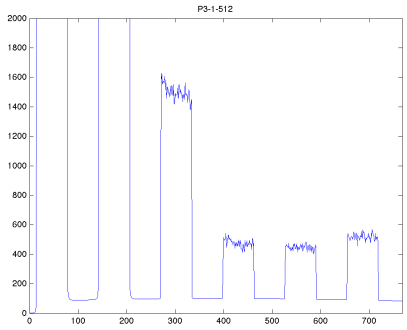


(a) convolved with PSF-1 (b) selected profile

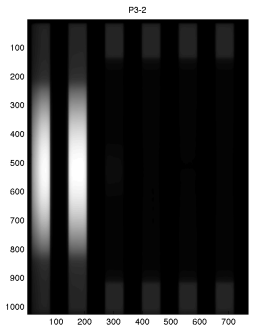


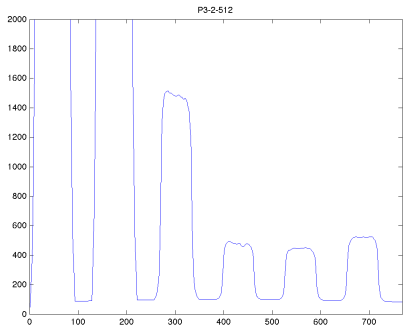


(c) convolved with PSF-2 (d) selected profile

Figure 3-5 convolved image

The final step is to deconvolve the blurred and noisy image using the corresponding PSF. The image can be restored to the original image when there is no noise added. However, the noise can not be removed from the blurred image because we don't have a model of it. Using the Wiener and Richardson-Lucy deconvolution, the noise can be suppressed to some extent. Two typical line profiles are shown in Fig. 3-6, low noise and medium noise. The root mean square error (RMSE) for different methods is shown in the Table 3.

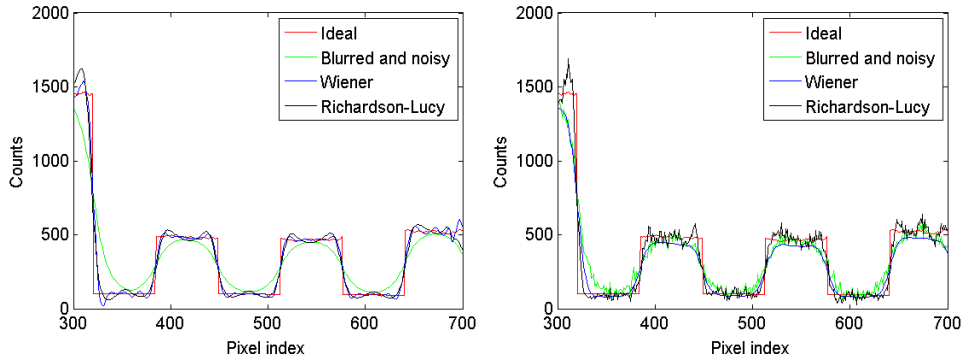


(a) Low Noise (SNR=80dB) (b) Medium Noise (SNR=40dB)

Figure 3-6 The deconvolved line profiles

The line profiles (perpendicular to the orientation of blockers) of the ground truth and for different scatter estimation methods are shown in above. The Ideal means ground truth without blur and noise, the Blurred and noisy means measured for direct scatter estimation, the Wiener means after Wiener deconvolution of the measured data and the Richardson-Lucy means after Richardson-Lucy deconvolution of the measured data.

Table 3-1 RMSE of the profile of blurred image

| SNR (dB) | 160 | 80 | 40 | 20 | 10 |
|---|---|---|---|---|---|
| PSF-1 | 0 | 30 | 151 | 303 | 605 |
| PSF-2 | 45 | 53 | 130 | 240 | 466 |
| PSF-3 | 82 | 82 | 115 | 200 | 393 |
| PSF-4 | 110 | 114 | 201 | 355 | 686 |
| PSF-5 | 130 | 136 | 187 | 282 | 498 |

Table 3-2 RMSE of the profile of deblurred image (Wiener)

| SNR (dB) | 160 | 80 | 40 | 20 | 10 |
|---|---|---|---|---|---|
| PSF-1 | 0 | 28 | 77 | 89 | 93 |
| PSF-2 | 1 | 8 | 18 | 26 | 37 |
| PSF-3 | 4 | 9 | 27 | 31 | 31 |
| PSF-4 | 18 | 25 | 34 | 34 | 33 |
| PSF-5 | 48 | 36 | 36 | 36 | 37 |

Table 3-3 RMSE of the profile of deblurred image (Richardson-Lucy)

| SNR (dB) | 160 | 80 | 40 | 20 | 10 |
|---|---|---|---|---|---|
| PSF-1 | 0 | 30 | 113 | 216 | 431 |
| PSF-2 | 0 | 30 | 114 | 214 | 422 |
| PSF-3 | 0 | 30 | 96 | 130 | 343 |
| PSF-4 | 0 | 30 | 90 | 128 | 275 |
| PSF-5 | 0 | 30 | 91 | 177 | 308 |

The RMSE values of estimated scatter using different methods are summarized In Fig. 3-7. The direct method suffers from the increased width of PSF and increased noise (Blue bars). After either Wiener or Richardson-Lucy deconvolution, the scatter estimation performance is significantly improved. In general, Wiener is robust to the change of noise levels and Richardson-Lucy seems to work well with the wide PSF. The deconvolution methods can achieve from as high as 20-fold improvement (Narrow PSF and Low noise) to a typical 4-fold improvement (Medium PSF and Medium noise).

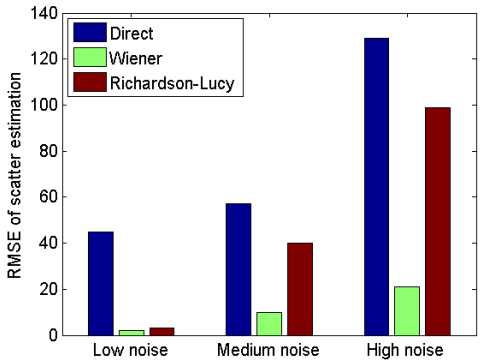


(a) Narrow PSF (FWTM = 6.2mm)

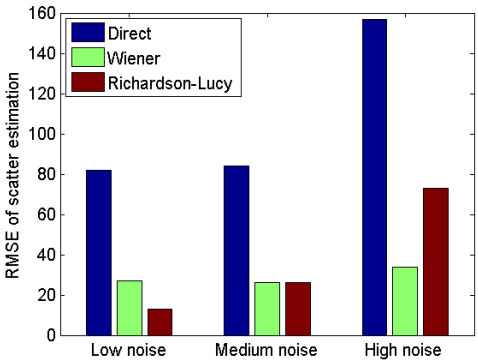


(b) Medium PSF (FWTM = 12.4mm)

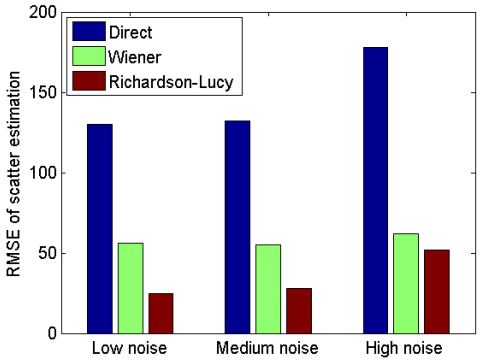


(c) Wide PSF (FWTM = 24.8mm)

Table 3-4 The root mean square error (RMSE)

The RMSE of estimated scatter using different methods are shown in above (Direct: using signal in the blocked region to estimate scatter directly; Wiener: Wiener deconvolution followed by direct scatter estimation; Richardson-Lucy: Richardson-Lucy deconvolution followed by direct scatter estimation; under different blurring and noise conditions. (Note the inverse filtering is very sensitive to noise and omitted here.)

## 3.6 Conclusion

We investigated several deconvolution methods to recover the scatter signal in the blocked region for blocker-based scatter correction for CBCT. Our simulation results demonstrate that Wiener and Richardson-Lucy deconvolution can significantly improve the scatter estimation compared to the direct method. Due to the blurring effect, the scatter signal in the blocked region is contaminated by the primary signal in the unblocked region. The direct use of the signal in the blocked region to estimate scatter ("direct method") leads to large RMSE, whose values increase with the increased width of PSF and increased noise. The inverse filtering is very sensitive to noise and practically useless. The Wiener and Richardson-Lucy deconvolution methods significantly improve scatter estimation compared to the direct method. For a typical medium PSF and medium noise condition, both methods (~20) can achieve 4-fold improvement over the direct method (~80). The Wiener method deals better with large noise and Richardson-Lucy works better on large PSF.

# Chapter 4

## A slanted-edge experiment

We performed an slanted-edge experiment to model the detector response function (DRF) for a flat panel detector (FPD). The slanted-edge method [41,42] can be used to estimate the detector response function (DRF), i.e. point spread function [43,44]. A lead sheet with sharp and straight edge will be placed directly on the top of the FPD to avoid off-focal radiation and environmental scatter. A uniform incident fluence on the measured area will be assured by calibration. The angle of the edge is not parallel to the u or v axis, but slanted slightly (<5°). This allows the gradient of the edge to be measured at various phases relative to the detector element and generates an oversampled edge profile as shown in Fig. 3-1, which will provide extra high frequency response information. The novelty of this work is to investigate the effectiveness of deconvolution methods on improving blocker-based CBCT scatter estimation. Due to the blurring effect from the X-ray source distribution and the detector response, the scatter signal in the blocked region is contaminated by the primary signal in the unblocked region, which leads to incorrect estimate of scatter in the whole projection image if no empirically adjustments were conducted. This work will provide a theoretically sound and practical solution to this problem and preliminary evidence that to what extent deconvolution methods can work. The purpose of this experiment is to measure the line spread function (LSF) and the modulation transfer function (MTF) of the projection image, then estimate the point spread function (PSF) and use them to deconvolve the original image to decrease the impact of the detector response effect.

4.1 slanted-edge method

Figure 4-1 and Figure 4-2 show the projection image of a slanted lead plate and its edge profile. The ideal edge profile has a sharp corner but the real edge profile doesn't (shown in Fig. 4-1(c)). Our goal of this experiment is to process the projection image to make the edge profile of the image sharp at the corner.

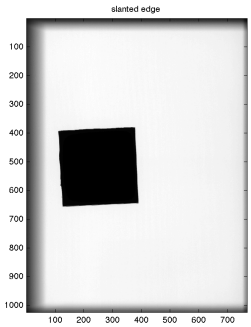


(a) slanted edge

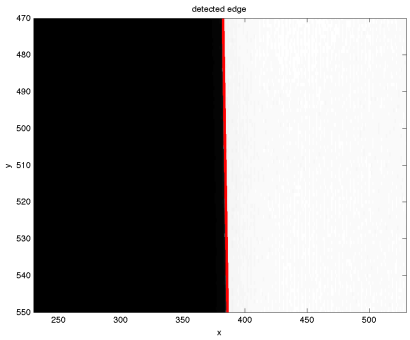


(b) detected edge

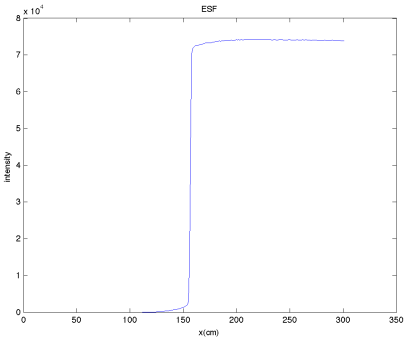


(c) estimated ESF

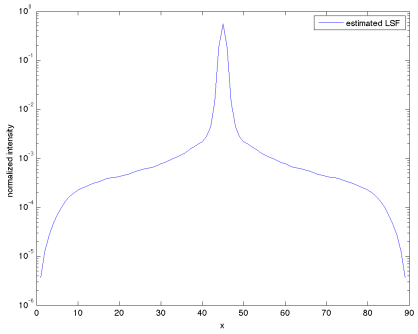


(d) estimated LSF

Figure 4-1 modeling LSF

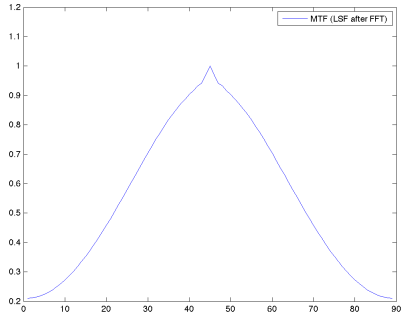


(a) estimated MTF

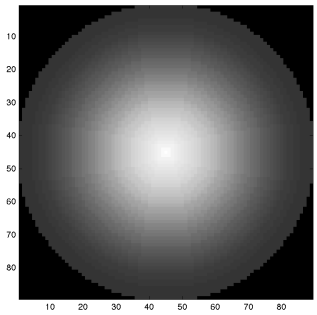

(b) estimated 2D MTF

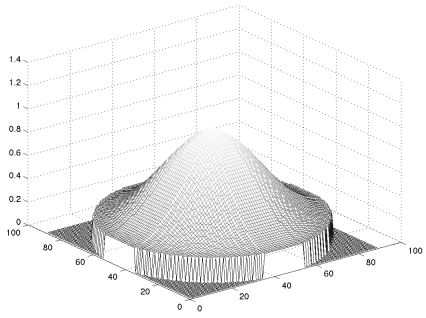

(c) estimated 3D MTF

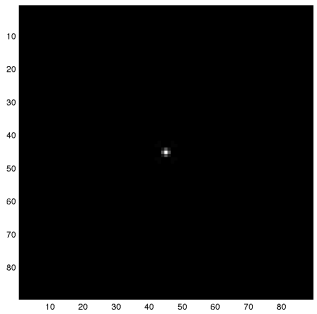

(d) estimated 2D PSF

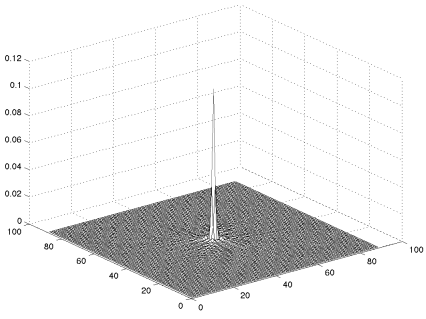

(e) estimated 3D PSF

Figure 4-2 clculating PSF

4.2 Results of differdent LSF

We compared three kinds of methods to drive the LSF and PSF. The estimated LSF and PSF were obtained from the experiment as shown in Fig. 4-3. The fitted LSF and PSF were obtained by fitting the estimated LSF to the Eq. (3.4) and Eq. (3.5). The parametric LSF and PSF were obtained from the the Eq. (3.4) and Eq. (3.5) using the parameters in the reference [34]. The dotted lines are the corresponding LSF derived from the PSF. From the Fig. 4-4, we conclude that the estimated LSF is close to the parametric LSF. The fitted LSF has some differences from the esimtaed LSF, which is caused by the fitting method  we use. The results of the deconvolution for the three kinds of PSF are shown in the Fig. 4-4. (a) and (b) are estimated PSF. (c) and (d) are parametirc PSF. (e) and (f) are fitted PSF. The RMSE for the profile of blurred image is 575. It became 1000, 55, 57 for the three PSF.

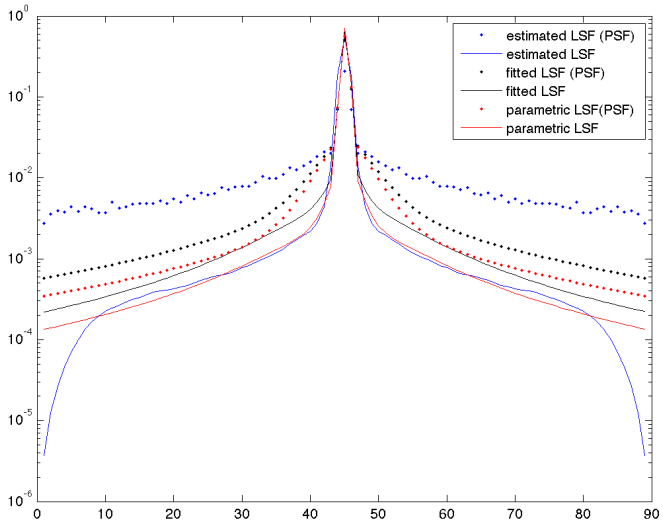


Figure 4-3  comparison of LSF and PSF

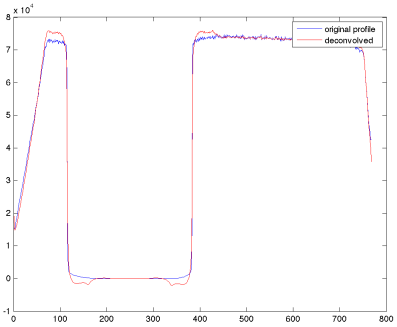


(a) deconvolved image

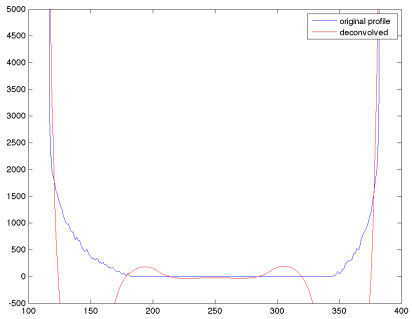


(b) region of interest

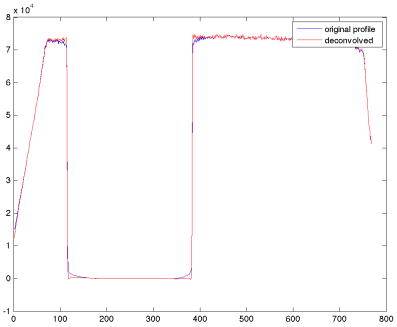


(c) deconvolved image

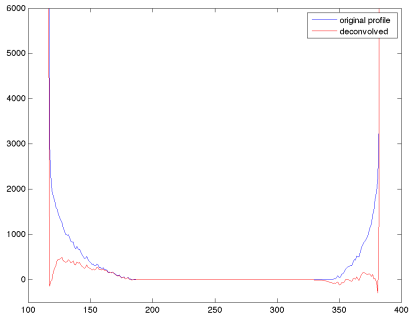


(d) region of interest

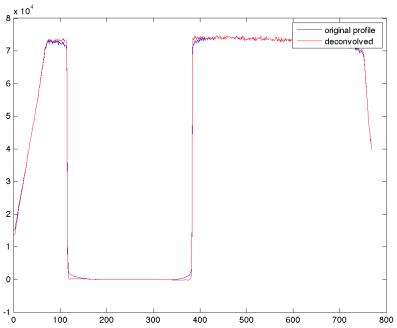


(e) deconvolved image

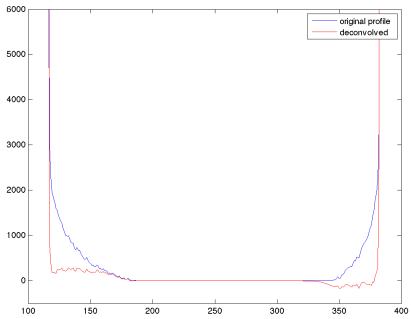


(f) region of interest

Figure 4-4 profile comparison after deconvlolution

## 4.3 Conclusion

In this chapter, we investigated the deconvolution method to remove the detecor response effect in the slanted-edge experiment. The PSF are derived from the slanted image using parametric model and then deconvolve the original projection image. Our results show that the slanted-edge method is effective to derive LSF and PSF for the flat panel detector, and the deconvolution method can significantly eliminate the detector response effect.

The penumbra effect is magnified by the blocker, which is also an important effect for blurring the image. We also tried to get the PSF of the projection image from the moving blocker method. However, the width of the lead strps is too small to contain the full information of PSF. A blind-deconvolution method have been proposed and will be implemented to see the performance.

# Chapter 5

## Summary

In summary, the results of reconstruction image and the CT number demonstrated that the moving blocker method can estimate the scatter signal in projection data, reduce the imaging dose, and simultaneously obtain complete volumetric information within the FOV. In the moving blocker methods, the signal detected in the blocked region is deemed scatter through an ideal projection assumption and used to estimate scatter in the unblocked region. The image reconstructed by the scatter corrected projection data from the unblocked regions.

However, the accuracy of the scatter correction using the moving blocker method is limited by the detector response effect and the penumbra effect. Then we proposed several deconvolution methods to improve the accuracy of the scatter correction and implemented a simulation study. The results of the simulation demonstrated that the deconvolution method can be used to deblur the projection image. To implement the deconvolution method, we proposed a slanted-edge experiment to derive the LSF and PSF using a parametric model. The results of the experiment showed that with good PSF estimation, the deconvolution method can significantly eliminate the detector response effect. Therefore, the moving blocker system with deconvolution method can generate high quality CBCT image. The high quality image can improve anatomical visualization and dose calculation accuracy in the treatment position, which are essential for the adaptive radiation therapy.

References

1. Yang Y, Schreibmann E, Li T, Wang C, Xing L. Evaluation of on-board kv cone beam ct (cbct)-based dose calculation. Phys Med Biol 2007;52:685-705.

2. Yoo S, Yin FF. Dosimetric feasibility of cone-beam ct-based treatment planning compared to ct-based treatment planning. Int J Radiat Oncol Biol Phys 2006;66:1553-1561.

3. van Zijtvetd M, Dirkx M, Heijmen B. Correction of conebeam ct values using a planning ct for derivation of the "dose of the day". Radiotherapy and Oncology 2007;85:195-200.

4. Siewerdsen JH, Jaffray DA. Cone-beam computed tomography with a flat-panel imager: Magnitude and effects of x-ray scatter. Med Phys 2001;28:220-231.

5. Neitzel U. Grids or air gaps for scatter reduction in digital radiography: A model calculation. Med Phys 1992;19:475-481.

6. Sorenson JA, Floch J. Scatter rejection by air gaps: An empirical model. Med Phys 1985;12:308-316.

7. Persliden J, Carlsson GA. Scatter rejection by air gaps in diagnostic radiology. Calculations using a monte carlo collision density method and consideration of molecular interference in coherent scattering. Phys Med Biol 1997;42:155-175.

8. Siewerdsen JH, Moseley DJ, Bakhtiar B, Richard S, Jaffray DA. The influence of antiscatter grids on soft- tissue detectability in cone-beam computed tomography with flat-panel detectors. Med Phys 2004;31:3506- 3520.

9. Endo M, Tsunoo T, Nakamori N, Yoshida K. Effect of scattered radiation on image noise in cone beam ct. Med Phys 2001;28:469-474.

10. J. Wiegert, M. Bertram, D. Schafer, N. Conrads, J. Timmer, T. Aach, Rose G. Performance of standard fluoroscopy anti-scatter grids in flat detector based cone beam ct. Proc SPIE Medical Imaging 2004;5368:67- 68.
11. Boone JM, Seibert JA. Monte carlo simulation of the scattered radiation distribution in diagnostic radiology. Med Phys 1988;15:713-720.
12. Malusek A, Seger MM, Sandborg M, Alm Carlsson G. Effect of scatter on reconstructed image quality in cone beam computed tomography: Evaluation of a scatter-reduction optimisation function. Radiat Prot Dosimetry 2005;114:337-340.
13. Jarry G, Graham SA, Moseley DJ, Jaffray DJ, Siewerdsen JH, Verhaegen F. Characterization of scattered radiation in kv cbct images using monte carlo simulations. Med Phys 2006;33:4320-4329.
14. Zbijewski W, Beekman FJ. Efficient monte carlo based scatter artifact reduction in cone-beam micro-ct. IEEE Trans Med Imaging 2006;25:817-827.
15. Spies L, Evans PM, Partridge M, Hansen VN, Bortfeld T. Direct measurement and analytical modeling of scatter in portal imaging. Med Phys 2000;27:462-471.
16. Rinkel J, Gerfault L, Esteve F, Dinten JM. A new method for x-ray scatter correction: First assessment on a cone-beam ct experimental setup. Phys Med Biol 2007;52:4633-4652.
17. Li H, Mohan R, Zhu XR. Scatter kernel estimation with an edge-spread function method for cone-beam computed tomography imaging. Phys Med Biol 2008;53:6729-6748.
18. Boone JM, Seibert JA. An analytical model of the scattered radiation distribution in diagnostic radiology. Med Phys 1988;15:721-725.
19. Seibert JA, Boone JM. X-ray scatter removal by deconvolution. Med Phys 1988;15:567-575.

20. Ning R, Tang X, Conover D. X-ray scatter correction algorithm for cone beam ct imaging. Med Phys 2004;31:1195-1202.

21. Siewerdsen JH, Daly MJ, Bakhtiar B, Moseley DJ, Richard S, Keller H, Jaffray DA. A simple, direct method for x-ray scatter estimation and correction in digital radiography and cone-beam ct. Med Phys 2006;33:187-197.

22. Zhu L, Bennett NR, Fahrig R. Scatter correction method for x-ray ct using primary modulation: Theory and preliminary results. IEEE Trans Med Imaging 2006;25:1573-1587.

23. Liu X, Shaw CC, Wang T, Chen L, Altunbas MC, Kappadath SC. An accurate scatter measurement and correction technique for cone beam breast ct imaging using scanning sampled measurement (ssm) technique. Proc Soc Photo Opt Instrum Eng 2006;6142:6142341-6142347.

24. Zhu L, Strobel N, Fahrig R. X-ray scatter correction for cone-beam ct using moving blocker array. Proceedings of the SPIE 2005;5745:251-258.

25. Zhu L, Xie Y, Wang J, Xing L. Scatter correction for cone-beam ct in radiation therapy. Med Phys 2009;36:2258-2268.

26. Zhu L, Wang J, Xie YQ, Starman J, Fahrig R, Xing L. A patient set-up protocol based on partially blocked cone-beam ct. Technology in Cancer Research & Treatment 2010;9:191-198.

27 R. Ning, X. Tang, and D. Conover, “X-ray scatter correction algorithm for cone beam CT imaging,” Med. Phys. 31, 1195–1202 (2004).

28 J. H. Siewerdsen, M. J. Daly, B. Bakhtiar, D. J. Moseley, S. Richard, H. Keller, and D. A. Jaffray, “A simple, direct method for x-ray scatter estimation and correction in digital radiography and cone-beam CT,” Med. Phys. 33, 187–197 □2006□.

29. Yan H, Mou X, Tang S, Xu Q, Zankl M. Projection correlation based view interpolation for cone beam ct: Primary fluence restoration in scatter measurement with a moving beam stop array. Phys Med Biol 2010;55:6353-6375

30. Wang J, Mao W, Solberg T. Scatter correction for cone-beam computed tomography using moving blocker strips: A preliminary study. Med Phys 2010;37:5792-5800.

31. Luo Ouyang, Kwang Song, and Jing Wang A moving blocker system for cone-beam computed tomography scatter correction, Medical Physics 40, 071903 (2013); doi: 10.1118/1.4811086

32. Ritschl L, Fahrig R, Knaup M, Maier J, Kachelrieß M. Robust primary modulation-based scatter estimation for cone-beam CT. Med Phys. 2015 Jan;42(1):469. doi: 10.1118/1.4903261.

33. H. Gao, L. Zhu, and R. Fahrig, “Modulator design for x-ray scatter correction using primary modulation: Material selection,” Med. Phys. 37, 4029–4037 (2010).

34. G.-H. Chen, J. Tang, and S. Leng, “Prior image constrained compressed sensing (PICCS): A method to accurately reconstruct dynamic CT images from highly undersampled projection data sets,” Med. Phys. 35, 660–663 (2008).

35. J. Song, Q. H. Liu, G. A. Johnson, and C. T. Badea, “Sparseness prior based iterative image reconstruction for retrospectively gated cardiac micro-CT,” Med. Phys. 34, 4476–4483 (2007).

36. E. Y. Sidky and X. Pan, “Image reconstruction in circular cone-beam computed tomography by constrained, total-variation minimization,” Phys. Med. Biol. 53, 4777–4807 (2008).

37. E. J. Candes, J. Romberg, and T. Tao, “Robust uncertainty principles: Exact signal reconstruction from highly incomplete frequency informa- tion,” IEEE Trans. Inf. Theory 52, 489–509 (2006).

38. R. L. Siddon, “Fast calculation of the exact radiological path for a three- dimensional CT array,” Med. Phys. 12, 252–255 (1985).

39. H. Yu and G. Wang, “Compressed sensing based interior tomography,” Phys. Med. Biol. 54, 2791–2805 (2009).

40. Lazos, Dimitrios, and Jeffrey F. Williamson. "Impact of flat panel-imager veiling glare on scatter-estimation accuracy and image quality of a commercial on-board cone-beam CT imaging system." Medical physics 39.9 (2012): 5639-5651.

41. Photography–Electronic Still Picture Cameras–Resolution Measurements, ISO Standard 12233: 2000.

42. Masaoka K, Yamashita T, Nishida Y, Sugawara M.Modified slanted-edge method and multidirectional modulation transfer function estimation. Opt Express. 2014 Mar 10;22(5):6040-6. doi: 10.1364/OE.22.006040.

43. G. Poludniowski, P. M. Evans, A. Kavanagh, and S. Webb, “Removal and effects of scatter-glare in cone- beam CT with an amorphous-silicon flat- panel detector,” Phys. Med. Biol. 56, 1837–1851 (2011)

44. Lazos D, Williamson JF. Impact of flat panel-imager veiling glare on scatter-estimation accuracy and image quality of a commercial on-board cone-beam CT imaging system. Med Phys. 2012 Sep;39(9):5639-51. doi: 10.1118/1.4747260.

45. Dong X, Niu T, Jia X, Zhu L. Relationship between x-ray illumination field size and flat field intensity and its impacts on x-ray imaging. Med Phys. 2012 Oct;39(10):5901-9. doi: 10.1118/1.4750054.

46. C. Kimme-Smith, L. W. Bassett, and R. H. Gold, “Focal spot size measurements with pinhole and slit for microfocus mammography units,” Med. Phys. 15(3), 298–303 (1988).

47. P. Russo and G. Mettivier, “Method for measuring the focal spot size of an x-ray tube using a coded aperture mask and a digital detector,” Med. Phys. 38(4), 2099–2115 (2011).

48. Richardson, William Hadley (1972). "Bayesian-Based Iterative Method of Image Restoration". JOSA 62 (1): 55–59.

49. Lucy, L. B. (1974). "An iterative technique for the rectification of observed distributions". Astronomical Journal 79 (6): 745–754.

50. Dey N, Blanc-Feraud L, Zimmer C, Roux P, Kam Z, Olivo-Marin J-C, Zerubia J. Richardson-Lucy algorithm with total variation regularization for 3D confocal microscope deconvolution. Microsc. Res. Techniq. 2006;69:260–266.

51. Laasmaa M, Vendelin M, Peterson P. Application of regularized Richardson–Lucy algorithm for deconvolution of confocal microscopy images. Journal of Microscopy 2011;243(Pt 2):124-140.

52. H. Lee, L. Xing, R. Lee, and B. P. Fahimian, “Scatter correction in cone- beam CT via a half beam blocker technique allowing simultaneous acquisi- tion of scatter and image information,” Med. Phys. 39, 2386–2395 (2012).

## Biographical Information

Cong Zhao received his B.E. degree in electric science and technology at the Huazhong University of Science and Technology, China in 2013. His research interests include computed-tomography (CT) reconstruction, CT scatter correction and positron emission tomography (PET) reconstruction. Upon receiving his master degree in May 2015, he will continue his education with a Ph.D. degree in the Physics Department at the University of Arlington.